Supporting Information

Cross et al. 10.1073/pnas.1115623109

SI Materials and Methods

HTS Screen for IRE1 Inhibitors. Screening of 238,287 commercially available chemicals and fractionated natural plant and fungal extracts using a modified Förster resonance energy transfer (FRET) assay for ref. 1 was carried out at the Institute of Chemistry and Cell Biology screening facility at Harvard. Briefly, reactions (10 μL) containing 4 nM hIRE1 in mammalian IRE1 reaction buffer (50 mM HEPES pH 7.2, 100 mM KOAc, 0.005% triton, 1 mM DTT) were treated with 20 μM library compounds followed by a 60-min incubation and then the addition of 10 μL of 2X (48 nM) IRE1 substrate (5′ AF647-CAUGUCCGCAGCGCAUG-BHQ3 3′) prior to fluorescence detection (excitation 612 nm, emission 670 nm) at 30 and 90 min in an Envision plate reader. We identified 2,627 inhibitors (2,627/238,286; 1.1%) among the whole set but eliminated the 1,877 from natural compound libraries from further consideration due to the facility imposed limitations in the secondary screening sample size. Among the 750 that were identified in the Marcus or commercial libraries, 205 were identified as H (high/strong), 233 as M (medium), 156 as W (weak), and 155 as XW (extra weak). Among the remaining compounds, 705 were supplied and rescreened in IRE1 RNase assay, and 99 of the available top hits were reordered as powders and retested in the IRE1 RNase assay and in a UPRE-Luciferase reporter assay.

Additional Cell Culture Procedures. For microscopy, AR42J cells treated with dexamethasone and 4μ8C were fixed after treatment by addition of 2X fixation solution (4% paraformaldehyde, 5% glutaraldehyde in 0.2M PBS, pH 7.2–7.4, made freshly), incubated for 5 min at 37 °C. Cells were then harvested by scraping, washed in 1X fixation solution and subjected to TEM. Mutant and wild type human IRE1α were cloned into pBABE housing a puromycin resistance cassette and introduced into Ire1$\alpha^{-/-}$ cells by retroviral transduction.

FRET Assays for RNase L Activity. RNase L activity was determine by FRET as described (2). Briefly, purified recombinant human RNase L (24 nM) was preincubated with varying concentration of 4μ8C or sunitinib for 5 min on ice followed by the addition of 2-5A (3 nM) and FRET probe (100 nM) in cleavage buffer (25 mM Tris-HCl, pH 7.4; 100 mM KCl; 10 mM MgCl2 and 7 mM 2-mercaptoethanol) for 10 min on ice and incubated for 60 min at 22 °C. The FRET probe is a 36 nucleotide synthetic oligoribonucleotide with a fluorophore (6-FAM) at the 5′-terminus and a quencher BHQ-1 (black hole quencher-1) at the 3′-terminus derived from the intergenic region of respiratory syncytial virus (RSV) genomic RNA. The FRET RNA probe (6-FAM-UUA UCA AAU UCU UAU UUG CCC CAU UUU UUU GGU UUA-BHQ-1) is highly susceptible to cleavage by RNase L owing to the multiplicity of cleavage sites (UU or UA). When intact, the fluorophore (6-FAM) in the FRET probe is in proximity to the quencher (BHQ-1), and hence there is no emission due to FRET pairing. However, RNase L activation by 2-5A leads to the cleavage of RNA probe, which separates the fluorophore and quencher. Cleavage of the FRET probe was monitored by excitation at 485 nm and emission at 535 nm using a Victor-2 multiplate reader (Perkin Elmer). The experiment was performed in triplicate. The average light units (described as relative RNaseL activity) were plotted with standard deviations.

Size Exclusion Chromatography Analysis of IRE1 Labeling and Off-Rates. IRE1 (15 μm) was incubated with 4μ8C (100 μM) for 30 min prior to separation on a SEC5 150 column (Agilent) in 50 mM Tris pH 7.5, 100 mM NaCl, 10% glycerol, 1 mM DTT using an AKTA purifier FPLC. For in vitro off-rate determination, identical reactions were prepared and subject to separation on a SEC3 300 (Agilent) chromatography column on an Agilent LC1290 system with both absorbance and fluorescence detectors. The protein peak was collected, and then aliquots were reinjected at the indicated times after the preparative run. The ratio of the 4μ8C specific fluorescence emission (excitation 350 nm, emission 470 nm) signal to the peptide bond signal at 214 nm was determined for each time point. The half-life was then calculated using a nonlinear regression analysis.

Amylase Secretion Analysis. Secreted amylase was quantitated using Phadebas reagent (Magle AB), according to the manufacturers instructions. Briefly, 5×10^4 AR42J cells were seeded per well of a 96 well dish. Cells were incubated for 16 h to adhere and then treated with 100 nM dexamethasone, 4μ8C at varying concentrations or vehicle control. Growth media was then collected from 24-, 48-, or 96-h culture and incubated with the reagent at 37 °C for 15 min before quenching of the reaction with NaOH. Undigested starch dye was pelleted by centrifugation, and the released dye was quantitated by absorbance at 620 nm.

Time-Resolved NMR. *N*-((2-hydroxynaphthalen-1-yl)methylene) thiophene-2-sulfonamide (3.9 mg, 12 μmol) was dissolved in CD3CN (600 μL) in an oven-dried vial under a nitrogen atmosphere. The solution was transferred to an NMR tube and an initial ^{1}H NMR scan (number 0) taken on the CryoProbe Bruker Avance TCI ATM 500 spectrometer. At $t = 0$ D_2O (600 μL) was added via a syringe and the resulting solution mixed briefly. The multizg program was initiated on the spectrometer to record 53 scans at 60 s each. The lock and shim sequence lasted 3.0 min. The spectra displayed are scans 0, 5, 11, 16, 22, 28, 34, 40, and 46. Then, 7-hydroxy-4-methyl-8-((pyridin-2-ylimino)methyl)-2*H*-chromen-2-one (1.4 mg, 4.6 μmol) was dissolved in *d*6-DMSO (650 μL) in an oven-dried vial under a nitrogen atmosphere. An initial ^{1}H NMR scan 0 was taken on the same spectrometer (Cryo TCI ATM 500) followed by the addition of D_2O and a series of scans within the multizg program: 90 scans in 17.7 min; acquisition time 5 s each. The lock and shim sequence lasted 2.7 min and is included in the total time. Scans 0, 1, 11 21, 31, 41, 51, 61, 71, 81, and 91 are displayed.

Spectroscopy. Samples containing 20 μL of 25 mM compound were scanned first in absorbance wavelength scan mode or fluorescence (fixed excitation 350 nm, emission scan) mode in an EnSpire™ multifunction plate reader (Perkin Elmer).

Mass Spectrometry. The collected samples were dried and analyzed by MALDI-TOF mass spectrometry and nanoLC-ESI-MS/MS after resuspending in 0.1%FA. HPLC grade water, acetonitrile, formic acid, and trifluoroacetic acid were purchased from Fisher Scientific. DHB matrix was prepared by dissolving 10 mg dihydroxybenzoic acid (Sigma-Aldrich) in 1 mL of water/acetonitrile (50:50, vol/vol) containing 0.1% TFA.

MALDI-TOF mass spectrometry. Sample was mixed with DHB matrix at a ratio of 1:1 (vol/vol), and 2 μL of this mixture was spotted onto the MALDI sample plate. MALDI-TOF mass spectra were acquired with an Autoflex MALDI-TOF mass spectrometer (Bruker Daltonics) equipped with a nitrogen laser and operated in positive ion reflectron mode. The calibration was performed

externally using peptide calibration standard. Mass spectra were processed by flexAnalysis 3.0 software (Bruker Daltonics). A total of 200–800 laser shots were averaged per mass spectrum, the background was subtracted, and each spectrum was smoothed.

NanoLC-ESI-MS/MS mass spectrometry. NanoLC-ESI-MS/MS analysis was performed on an LTQ-Orbitrap hybrid mass spectrometer (Thermo Fisher Scientific) equipped with a nanoelectrospray ionization source (Jamie Hill Instrument Services) and an Eksigent nanoLC system (Eksigent Technologies) with a self-packed 75 μm × 12 cm reverse-phase column (Reprosil C18, 3 μm, Dr. Maisch GmbH) coupled directly to the mass spectrometer. Peptides were eluted by a gradient of 3–40% acetonitrile in 0.1% formic acid over 24 min. The mass spectrometer was operated in data-dependent mode to automatically switch between 60,000 resolution MS survey scans acquired in the Orbitrap mass analyzer and up to eight CID MS/MS scans on the most intense peaks from survey scans acquired in the LTQ mass analyzer. Automatic gain control target values were set to 500,000 for Orbitrap and 10,000 for LTQ. Orbitrap data were acquired in profile mode, and LTQ data were acquired in centroid mode. Mascot generic format files were generated from the raw data using DTA-SuperCharge 1.19 and searched using Mascot 2.2.1 (Matrix Science) against a database containing amino acid sequences of IRE1 protein and common contaminants with the following parameters: 15 ppm MS mass tolerance, 0.4 Da MS/MS mass tolerance, trypsin specificity with a maximum one missed cleavage allowed, variable oxidation (methionine), deamidation (asparagine and glutamine), and +C11H8O3 (lysine). The Mascot algorithm was instructed to score fragment ions resulting from loss of an inhibitor group. Sub 2 ppm mass accuracy was achieved with postacquisition calibration of MS data using trypsin autolytic peptide peaks identified in the first round of searching.

Docking and Molecular Dynamics Simulations ***Protein model preparation.*** Each system contained dimeric IRE1, bound to Mg^{2+}-complexed ADP, with initial coordinates extracted from Protein Data Bank (PDB) ID code 3P23. The protein and ligand were protonated and all ionizable groups of the protein were assigned their most probable charged states at neutral pH. Two loops with missing density in the crystal structure (residues 157–168 and 185–187) were built using the Modeller suite; 1,000 models were built and the lowest-energy conformations were subsequently refined with the DOPE module.

4μ8C docking. Initial 4μ8C-bound states at Lys599 and/or Lys907 were built using the Builder module in Pymol (http://www.pymol.org/), and then the conformations of 4μ8C were extensively diversified and optimized. Initially, the position of the protein and Mg^{2+}.ADP atoms were constrained, prior to 1,000 steps of steepest descent (SD) and adopted basis Newton–Raphson (ABNR) energy minimization. Subsequently, the angle of the axes of the two rotatable bonds in 4μ8C were rotated, and energy minimization was again performed. This was performed iteratively in 60° increments, so that all combinations of ranges between 0–360° were explored for both rotatable bonds, ensuring a thorough exploration of the configurational space available to 4μ8C within each binding site. For each minimized conformation, the coordinates and protein–4μ8C interaction energy were recorded. For the K907 site, a number of possible orientations were possible. The primary stabilizing contributions available were stacking interactions between the 4μ8C ring and Phe889, and hydrogen-bond (H-bond) formation between 4μ8C and the side chains of Asp885 and/or His910 (between 0–2 H bonds were possible in all docked structures analyzed). The conformation with the greatest interaction energy with the protein exhibited a stacking interaction and two H bonds. For the K599 site, in the presence of ADP, only one optimized conformation could be obtained, revealing H bonds between 4μ8C and ADP(*N9*) and the side chain of Asp711. Nevertheless, even in this conformation, the 4μ8C was extremely strained, suggesting it was unlikely to be possible to bind in the presence of ADP. In the absence of ADP, two bound, unstrained states could be identified, one of which revealed two H bonds to the side chains of Asp711 and His723. In each case, the conformations with the most favorable interaction energy between 4μ8C and protein were chosen for subsequent molecular dynamics calculations.

Simulation system setup. All systems were placed in a truncated octahedral box with a minimum of 1.5 nm between protein/ligand atoms and the box edges. Each system was solvated via superposition of a preequilibrated box of TIP3P water molecules. Sodium and chloride ions were added to neutralize any net charge in the system, with a total concentration of approximately 0.1 M to mimic physiological salt conditions. Before and after solvation, SD energy minimization was performed to relax any steric overlap between protein, ligand, and solvent. After obtaining the final minimized system, an equilibration stage was included to allow solvent to relax around the protein and/or ligand. To achieve this, position restrained dynamics were applied to all non-hydrogen atoms of the protein and lipid in three 0.5-ns MD simulation phases, gradually reducing the restraints in each phase. Finally, production simulations were run. Final system sizes were approximately 250,000 atoms, with approximately 70,000 water molecules.

Simulation and docking parameters. The CHARMM22/CMAP all-atom force field (3) was used to represent the protein, with parameters for 4μ8C adapted from the CHARMM CGenFF general force field for small drug-like molecules (4). Docking/optimization calculations were performed using CHARMM (5). All MD simulations were performed with the GROMACS 4.5.3 simulation package (6, 7). Simulations were carried out using the leap-frog algorithm with a 2-fs time step, and the LINCS algorithm (8) to constrain bond lengths. Electrostatic interactions were calculated with Particle-Mesh Ewald algorithm (9) and the real-space sum was cut off at 12 Å. Van der Waals interactions were smoothly switched off from 10 to 12 Å. The neighbor list was updated every 10 steps. All simulations were run in conditions of constant temperature (298 K) and pressure (1 atm) under periodic boundary conditions in all directions. The temperature coupling was performed with velocity rescaling using a stochastic term (10), and isotropic pressure coupling employed the Parrinello–Rahman barostat (11) with a coupling constant of 5 ps. For docking/optimization, nonbonded interactions were treated with an atom-based cutoff of 1.4 nm. Electrostatics used a distance-dependent dielectric, with a shifted potential going to zero beyond 1.2 nm. Van der Waals forces were switched from 1.0 to 1.2 nm.

Analysis. The analysis of the simulation trajectories was performed with the analysis tools provided in the GROMACS software package (http://www.gromacs.org), and VMD was used for graphical visualization (12). Graphs were constructed using Grace (http://plasma-gate.weizmann.ac.il/Grace/).

1. Wiseman RL, et al. (2010) Flavonol activation defines an unanticipated ligand-binding site in the kinase-RNase domain of IRE1. *Mol Cell* 38:291–304.
2. Jha BK, et al. (2011) Inhibition of RNase l and PKR by sunitinib impairs antiviral innate immunity. *J Biol Chem* 286:26319–26326.
3. MacKerell A, et al. (1998) All-atom empirical potential for molecular modeling and dynamics studies of proteins. *J Phys Chem B* 102:3586–3616.

4. Vanommeslaeghe K, et al. (2010) CHARMM general force field: A force field for drug-like molecules compatible with the CHARMM all-atom additive biological force fields. *J Comput Chem* 31:671–690.
5. Brooks BR, et al. (2009) CHARMM: The biomolecular simulation program. *J Comput Chem* 30:1545–1615.
6. Bjelkmar P, Larsson P, Cuendet MA, Hess B, Lindahl E (2010) Implementation of the CHARMM force field in GROMACS: Analysis of protein stability effects from correction maps, virtual interaction sites, and water models. *J Chem Theory Comput* 6:459–466.
7. Hess B, Kutzner C, van der Spoel D, Lindahl E (2008) GROMACS 4: Algorithms for highly efficient, load-balanced, and scalable molecular simulation. *J Chem Theory Comput* 4:435–447.
8. Hess B, Bekker H, Berendsen HJC, Fraaije JGEM (1997) LINCS: A linear constraint solver for molecular simulations. *J Comput Chem* 18:1463–1472.
9. Essmann U, et al.(1995) A smooth particle mesh Ewald method. *J Chem Phys*103:8577–8593.
10. Bussi G, Donadio D, Parrinello M (2007) Canonical sampling through velocity rescaling. *J Chem Phys* 126:014101.
11. Parrinello M, Rahman A (1981) Polymorphic transitions in single crystals: A new molecular dynamics method. *J Appl Phys* 52:7182–7190.
12. Humphrey W, Dalke A, Schulten K (1996) VMD: Visual molecular dynamics. *J Mol Graph* 14:33–38.

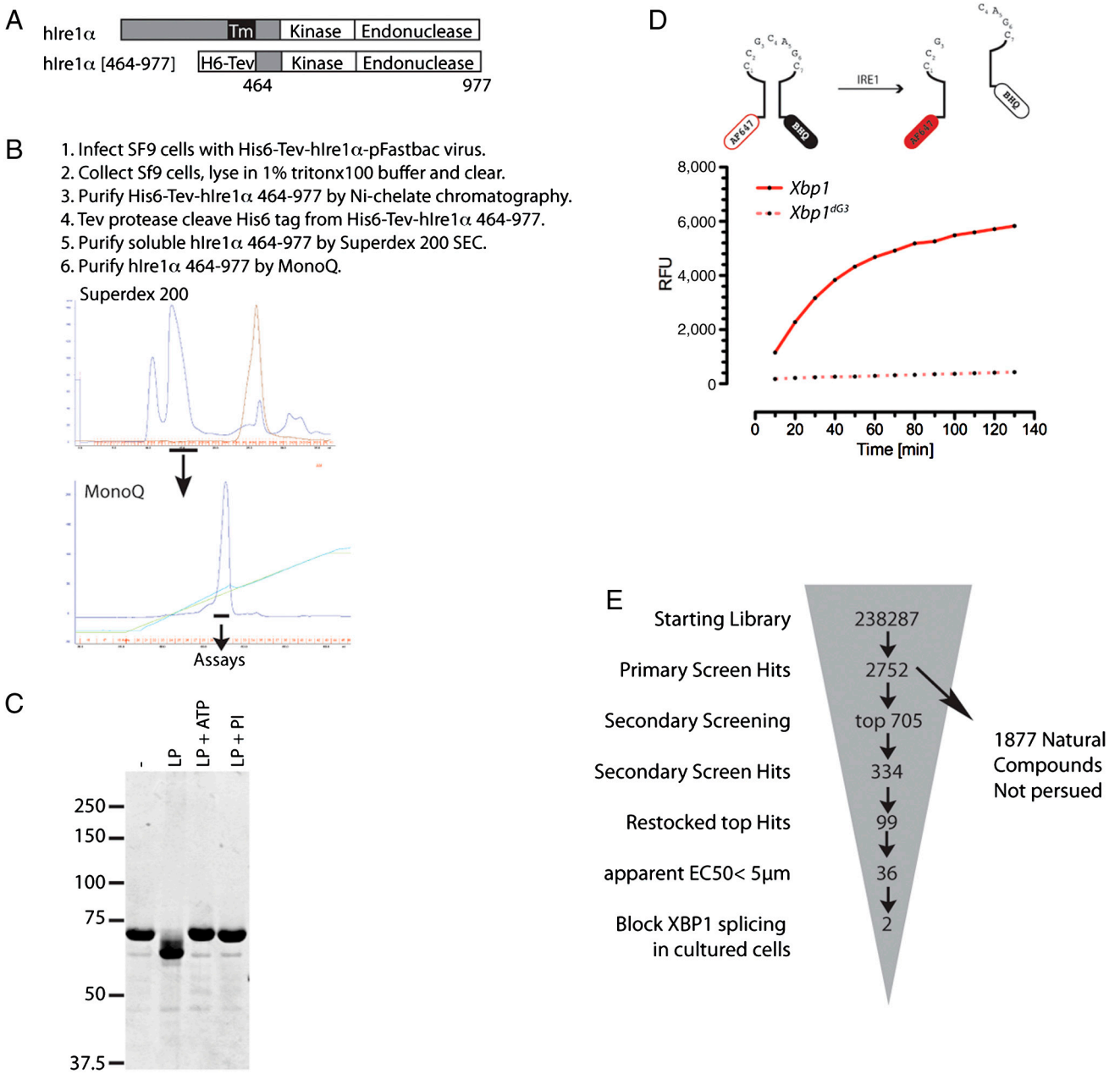

Fig. S1. A high-throughput screen for inhibitors of human IRE1. (*A*) Cartoon depicting the structure of the H6-Tev-IRE1α[464-977] protein in relation to full-length human IRE1α. (*B*) Six steps of purification of IRE1α[464-977] followed by plots of the absorbance at 280 nm during chromatography on Superdex 200 and Mono Q. Horizontal bars indicate the fractions that were used for the subsequent step (Superdex 200) or pooled for use in assays (Mono Q). (*C*) Coomassie blue stained gel of purified human IRE1α[464-977] untreated, treated with lambda phosphatase (LP) alone, with lambda phosphatase and ATP, or with lambda phosphatase and phosphatase inhibitors (PI). (*D*) Cartoon of the substrates used to detect IRE1 RNase activity via relief of FRET quenching and graph of fluorescence signal obtained in reactions containing purified IRE1α[464-977] and a BHQ *Xbp1*-AF647 tagged hairpin substrate (*Xbp1*) or a mutant substrate containing a deoxyguanosine substitution at the third base of the recognition loop (dG3). (*E*) Overview of HTS screening campaign.

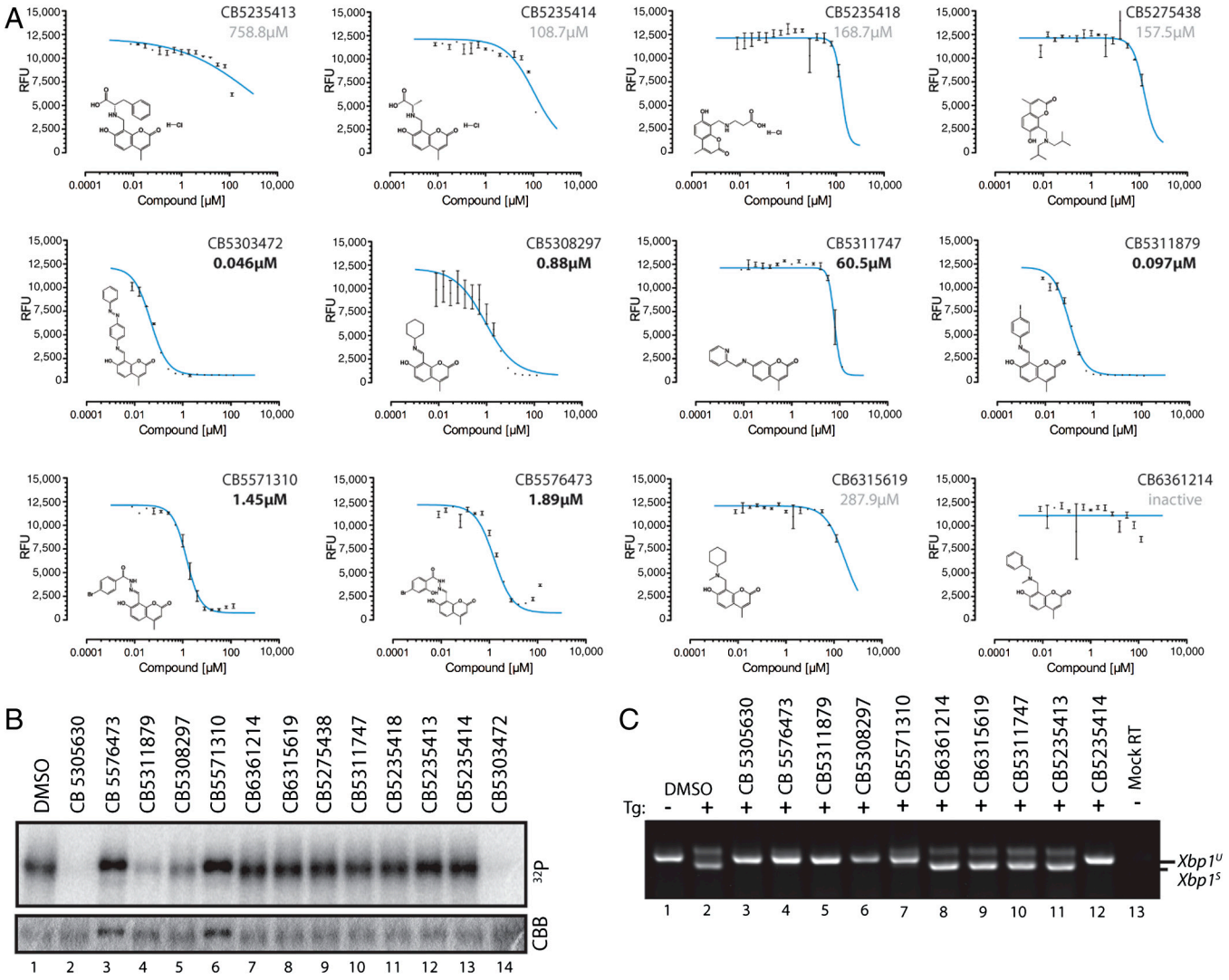

Fig. S2. SAR for hits identified by HTS. (*A*) In vitro structure-activity relationship analysis of coumarin inhibition of IRE1 determined using the FRET-derepression assay. Apparent IC_{50} values are shown in the inset to each graph. Half tone values indicate compounds with an IC_{50} lower than 100 μM. (*B*) Autokinase activity detected by radiograph of ^{32}P-labeled IRE1 subjected to PAGE following incubation with γ^{32}P-ATP in the presence of the absence, or presence of indicated compounds (8 μM). The lower panel displays the coomassie (CBB) stain of IRE1 from the same gel. (*C*) RT-PCR analysis of *Xbp1* splicing in MEFs treated with the indicated compounds (32 μM).

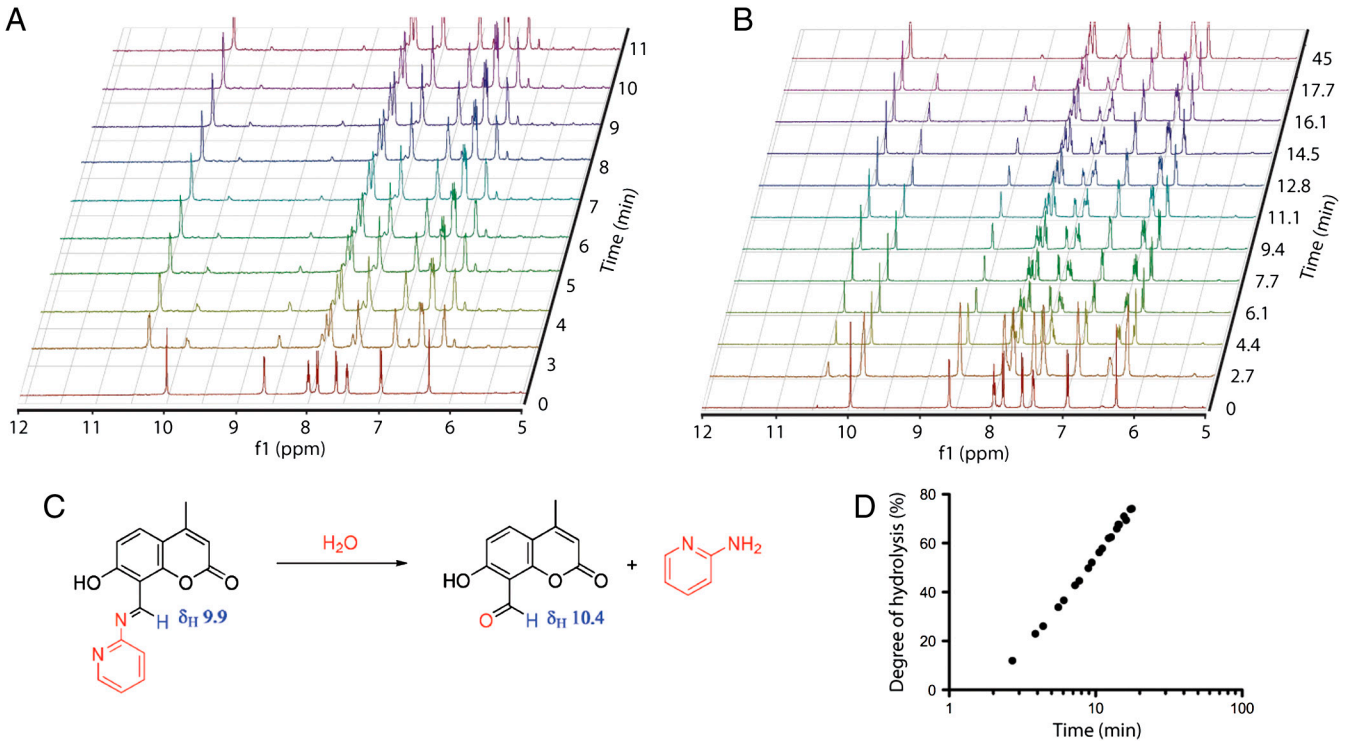

Fig. S3. Rapid hydrolysis of CB5305630 in aqueous conditions. (*A*) Time-resolved ^{1}H NMR spectra of CB5305630 in 20% D_2O. The premixed reaction mixture reaches 90% hydrolysis within 10 min. Spectra show $\delta = 4.75$ to 12.0 ppm only. (*B*) Time-resolved ^{1}H NMR spectra of CB5305630 in 12% D_2O in DMSO-d6; diffusion mixing. CB5305630 reached 80% hydrolysis within 40 min. Spectra show $\delta = 5.25$ to 12.0 ppm only. (*C*) Hydrolysis reaction scheme and resonances of the imine and carbaldehyde species. (*D*) Quantitation of the hydrolysis of CB5305630 to 8-formyl-7-hydroxy-4-methylcoumarin and 2-aminopyridine as in *B*.

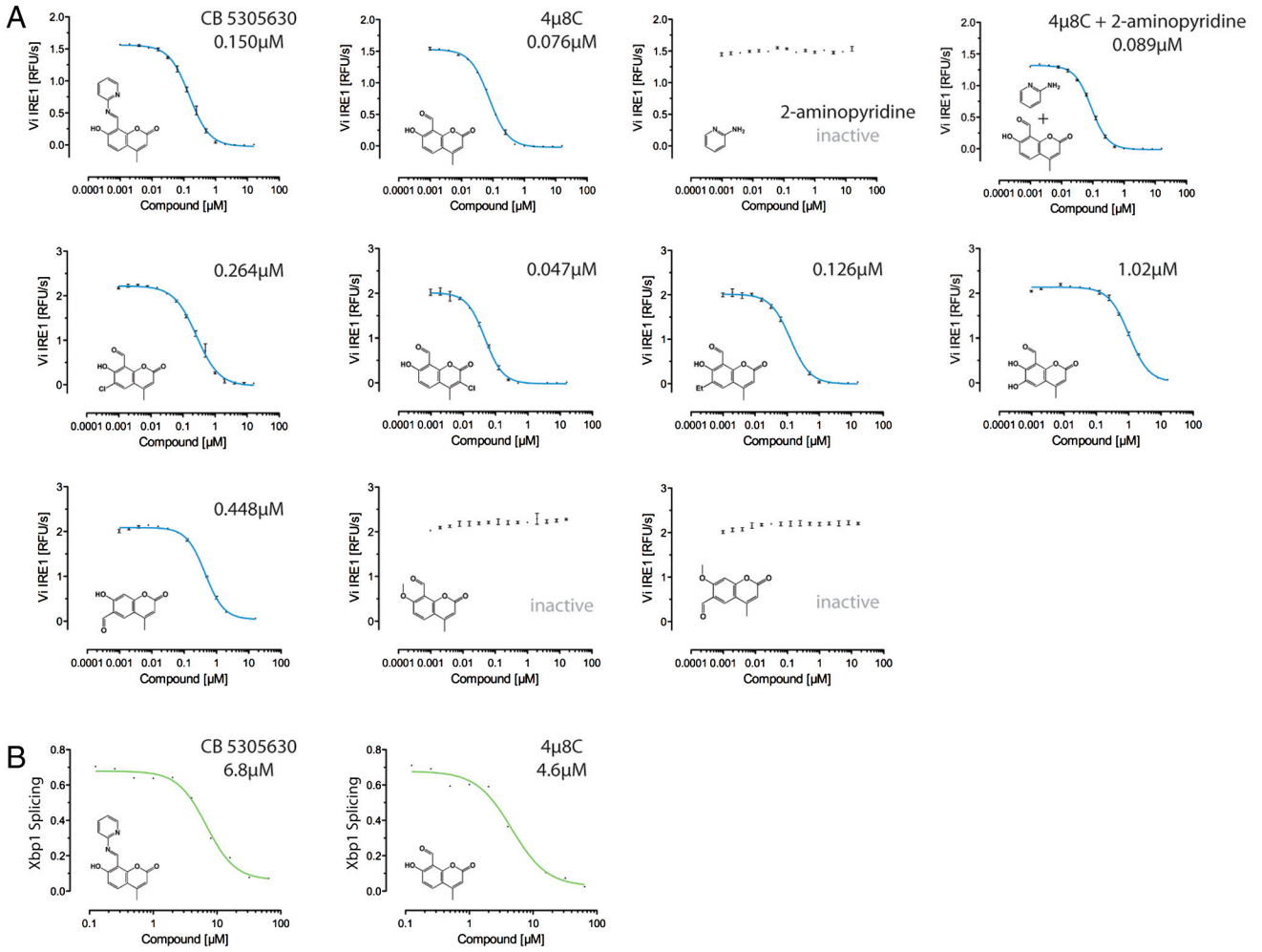

Fig. S4. Structural activity relationship analysis of 4μ8C. (*A*) Shown is the activity of the IRE1 RNase in vitro in the presence of the indicated concentrations of various compounds related in structure to 4μ8C using the FRET-derepression assay. Note in particular that 2-aminopyridine alone is inactive and that substitution of the ortho hydroxyl in 4μ8C and related compounds blocks inhibition. (*B*) Parallel concentration-response analysis of 8-formyl-7-hydroxy-4-methylcoumarin (4μ8C) and CB5305630 inhibition of Xbp1 splicing in vivo indicates that 4μ8C is the minimal active component in solutions of CB5305630.

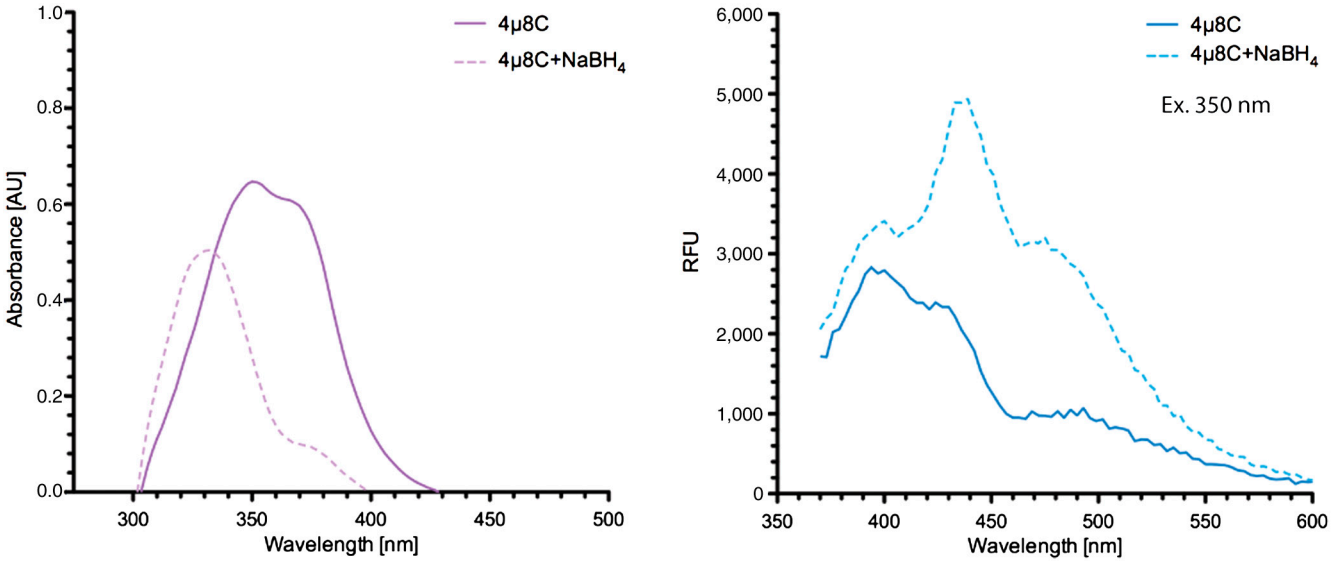

Fig. S5. Absorbance and fluorescence spectra of 4μ8C. (*Left*) Absorbance of 4μ8C before and after reduction with sodium borohydride. (*Right*) Emission spectra after excitation at 350 nm for 4μ8C before and after reduction with sodium borohydride. Note the shift in the absorbance to lower wavelengths and the shift to higher wavelengths with enhanced fluorescence in the emission spectrum of the reduced compound.

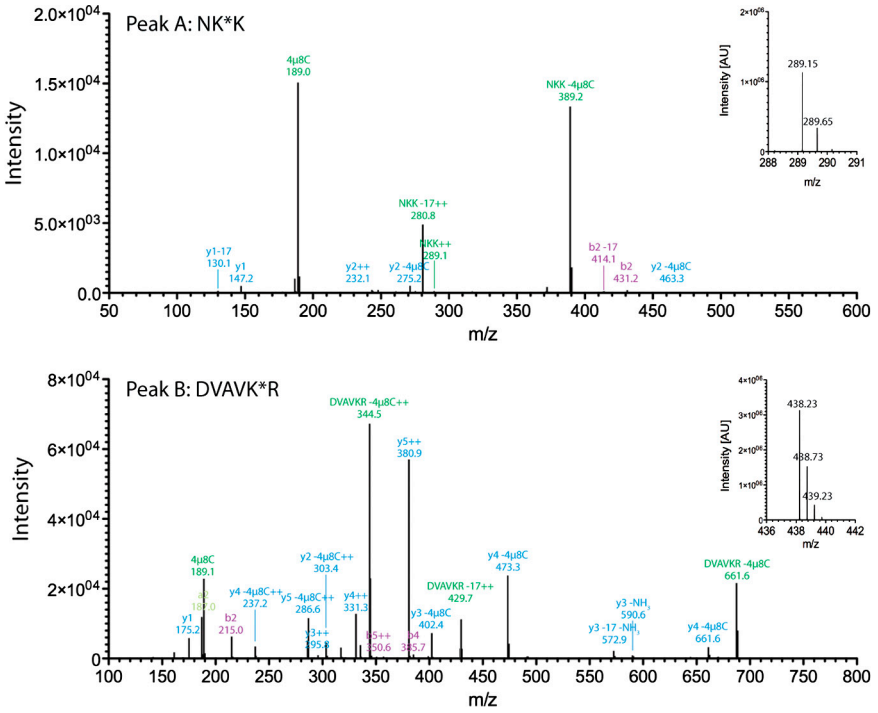

Fig. S6. ESI-MS/MS fragmentation spectra of modified IRE1 peptides. Collision-induced dissociation tandem mass spectra of 4μ8C-modified peptides [(*Upper*) NK*K peptide; (*Lower*) DVAVK*R peptide], identified earlier by MALDI-TOF MS. The small insets show MS spectra of doubly charged precursor ions selected for CID MS/MS experiments showing no significant cofragmentation with other ions. For both peptides, loss of the modification group upon CID is prominent (ions annotated as −4μ8C). The identification of K^{907} as the target of inhibitor was based on the presence of two high confidence discriminating ions (b2 at 431.2 *m*/*z* and b2-17 at 414.1 *m*/*z*) and the absence of ions specific to alternative site assignment within the specified mass tolerance (0.6 Th).

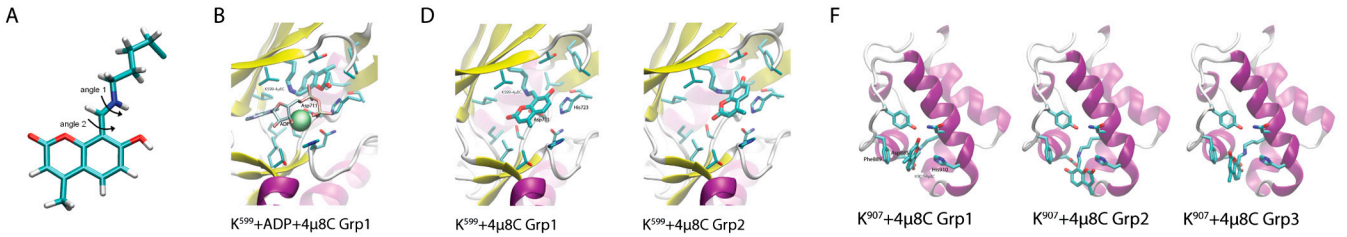

C

Angle 1 (deg)	Angle 2 (deg)	Inter. ene (kcal/mol)	NH - ADP(N9)	OH - D^{711}	Group
180	180	-20.2107	yes	yes	1
240	180	-20.2107	yes	yes	1
0	0	N/A	N/A	N/A	N/A
0	60	N/A	N/A	N/A	N/A
0	120	N/A	N/A	N/A	N/A
0	180	N/A	N/A	N/A	N/A
0	240	N/A	N/A	N/A	N/A
0	300	N/A	N/A	N/A	N/A
60	0	N/A	N/A	N/A	N/A
60	60	N/A	N/A	N/A	N/A
60	120	N/A	N/A	N/A	N/A
60	180	N/A	N/A	N/A	N/A
60	240	N/A	N/A	N/A	N/A
60	300	N/A	N/A	N/A	N/A
120	0	N/A	N/A	N/A	N/A
120	60	N/A	N/A	N/A	N/A
120	120	N/A	N/A	N/A	N/A
120	180	N/A	N/A	N/A	N/A
120	240	N/A	N/A	N/A	N/A
120	300	N/A	N/A	N/A	N/A
180	0	N/A	N/A	N/A	N/A
180	60	N/A	N/A	N/A	N/A
180	120	N/A	N/A	N/A	N/A
180	240	N/A	N/A	N/A	N/A
180	300	N/A	N/A	N/A	N/A
240	0	N/A	N/A	N/A	N/A
240	60	N/A	N/A	N/A	N/A
240	120	N/A	N/A	N/A	N/A
240	240	N/A	N/A	N/A	N/A
240	300	N/A	N/A	N/A	N/A
300	0	N/A	N/A	N/A	N/A
300	60	N/A	N/A	N/A	N/A
300	120	N/A	N/A	N/A	N/A
300	180	N/A	N/A	N/A	N/A
300	240	N/A	N/A	N/A	N/A
300	300	N/A	N/A	N/A	N/A

E

Angle 1 (deg)	Angle 2 (deg)	Inter. ene (kcal/mol)	NH - D^{711}	OH - H^{723}	Group
300	60	-87.654	yes	yes	1
240	180	-75.8794	no	no	2
0	0	N/A	N/A	N/A	N/A
0	60	N/A	N/A	N/A	N/A
0	120	N/A	N/A	N/A	N/A
0	180	N/A	N/A	N/A	N/A
0	240	N/A	N/A	N/A	N/A
0	300	N/A	N/A	N/A	N/A
60	0	N/A	N/A	N/A	N/A
60	60	N/A	N/A	N/A	N/A
60	120	N/A	N/A	N/A	N/A
60	180	N/A	N/A	N/A	N/A
60	240	N/A	N/A	N/A	N/A
60	300	N/A	N/A	N/A	N/A
120	0	N/A	N/A	N/A	N/A
120	60	N/A	N/A	N/A	N/A
120	120	N/A	N/A	N/A	N/A
120	180	N/A	N/A	N/A	N/A
120	240	N/A	N/A	N/A	N/A
120	300	N/A	N/A	N/A	N/A
180	0	N/A	N/A	N/A	N/A
180	60	N/A	N/A	N/A	N/A
180	120	N/A	N/A	N/A	N/A
180	180	N/A	N/A	N/A	N/A
180	240	N/A	N/A	N/A	N/A
180	300	N/A	N/A	N/A	N/A
240	0	N/A	N/A	N/A	N/A
240	60	N/A	N/A	N/A	N/A
240	120	N/A	N/A	N/A	N/A
240	240	N/A	N/A	N/A	N/A
240	300	N/A	N/A	N/A	N/A
300	0	N/A	N/A	N/A	N/A
300	120	N/A	N/A	N/A	N/A
300	180	N/A	N/A	N/A	N/A
300	240	N/A	N/A	N/A	N/A
300	300	N/A	N/A	N/A	N/A

G

Angle 1 (deg)	Angle 2 (deg)	Inter. ene (kcal/mol)	stack – F^{889}	NH - H^{910}	NH – D^{885}	OH – D^{885}	Group
60	300	-107.703	yes	no	yes	yes	1
180	300	-107.703	yes	no	yes	yes	1
180	0	-105.906	no	no	yes	yes	2
120	0	-100.298	no	yes	no	yes	2
120	300	-95.9984	yes	no	no	yes	3
60	0	-87.0481	yes	no	no	yes	3
60	60	-87.9712	yes	no	no	yes	3
120	60	-82.6969	no	no	no	yes	3
0	0	-78.4145	no	yes	no	no	4
0	60	-76.7883	no	yes	no	no	4
300	0	-76.9026	no	yes	no	no	4
0	300	-72.0565	yes	no	no	no	5
120	240	-73.287	yes	no	no	no	5
240	240	-75.0173	yes	no	no	no	5
240	300	-72.5524	yes	no	no	no	5
300	240	-72.4609	yes	no	no	no	5
300	300	-72.0596	yes	no	no	no	5
180	240	-59.1761	no	no	no	no	6
300	180	-53.0378	no	no	no	no	6
0	120	N/A	N/A	N/A	N/A	N/A	
0	180	N/A	N/A	N/A	N/A	N/A	
0	240	N/A	N/A	N/A	N/A	N/A	
60	120	N/A	N/A	N/A	N/A	N/A	
60	180	N/A	N/A	N/A	N/A	N/A	
60	240	N/A	N/A	N/A	N/A	N/A	
120	120	N/A	N/A	N/A	N/A	N/A	
120	180	N/A	N/A	N/A	N/A	N/A	
180	60	N/A	N/A	N/A	N/A	N/A	
180	120	N/A	N/A	N/A	N/A	N/A	
180	180	N/A	N/A	N/A	N/A	N/A	
240	0	N/A	N/A	N/A	N/A	N/A	
240	60	N/A	N/A	N/A	N/A	N/A	
240	120	N/A	N/A	N/A	N/A	N/A	
240	180	N/A	N/A	N/A	N/A	N/A	
300	60	N/A	N/A	N/A	N/A	N/A	
300	120	N/A	N/A	N/A	N/A	N/A	

Fig. S7. Docking of 4μ8C onto IRE1 K^{599} and K^{907}. (*A*) Rotatable bonds in 4μ8C explored during the docking analysis. (*B*) Docking of 4μ8C at IRE1 (PDB ID code 3P23) K^{599} by Schiff base in the presence of the Mg^{2+} ion and ADP. Image shows the only conformation group able to be assigned in this configuration. (*C*) Table showing docking criteria, including potential side-chain interactions, for 4μ8C at K^{599} + ADP. N/A indicates that optimizations in these configurations were impossible. (*D*) Conformation groups identified for docking of 4μ8C Schiff base at K^{599} in IRE1 without ADP present. (*E*) Table showing docking criteria, including potential side-chain interactions, for 4μ8C at K^{599} without ADP. Note the difference in internal energy (Inter. ene) for these configurations compared to those found for docking the compound in the ADP-bound IRE1, supporting our experimental observation that ADP and 4μ8C binding are likely to be mutually exclusive events. (*F*) Conformation groups identified for docking of 4μ8C by Schiff base at K^{907} of IRE1. (*G*) Table showing the docking criteria, including potential side-chain interactions, for 4μ8C at K^{907}. For molecular dynamic simulations, the conformation with the greatest internal energy was used as time = 0 ns. See *SI Materials and Methods* for more detail of these analyses.

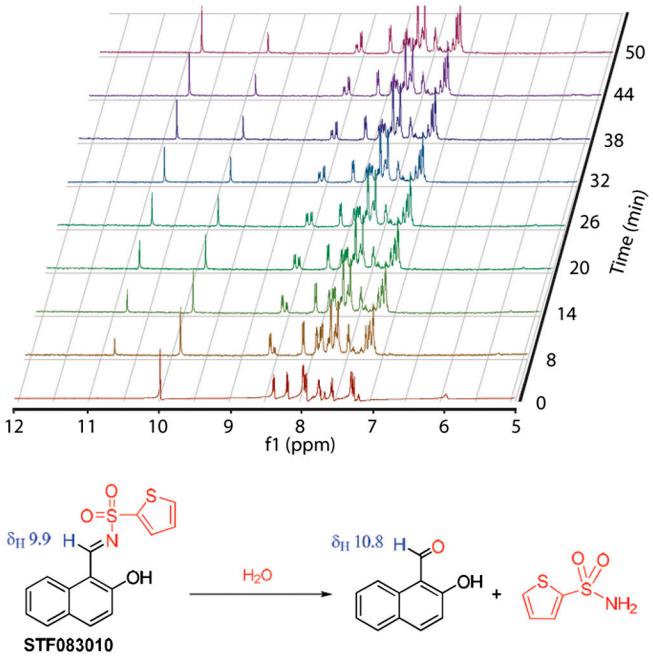

Fig. S8. Rapid hydrolysis of STF-083010 to a carbaldehyde in an aqueous environment. ^{1}H NMR of STF-083010 hydrolysis to a napthalene carbaldehyde in 50% D_2O in CD3CN. Spectra show $\delta = 5.0$ to 13.0 ppm only.

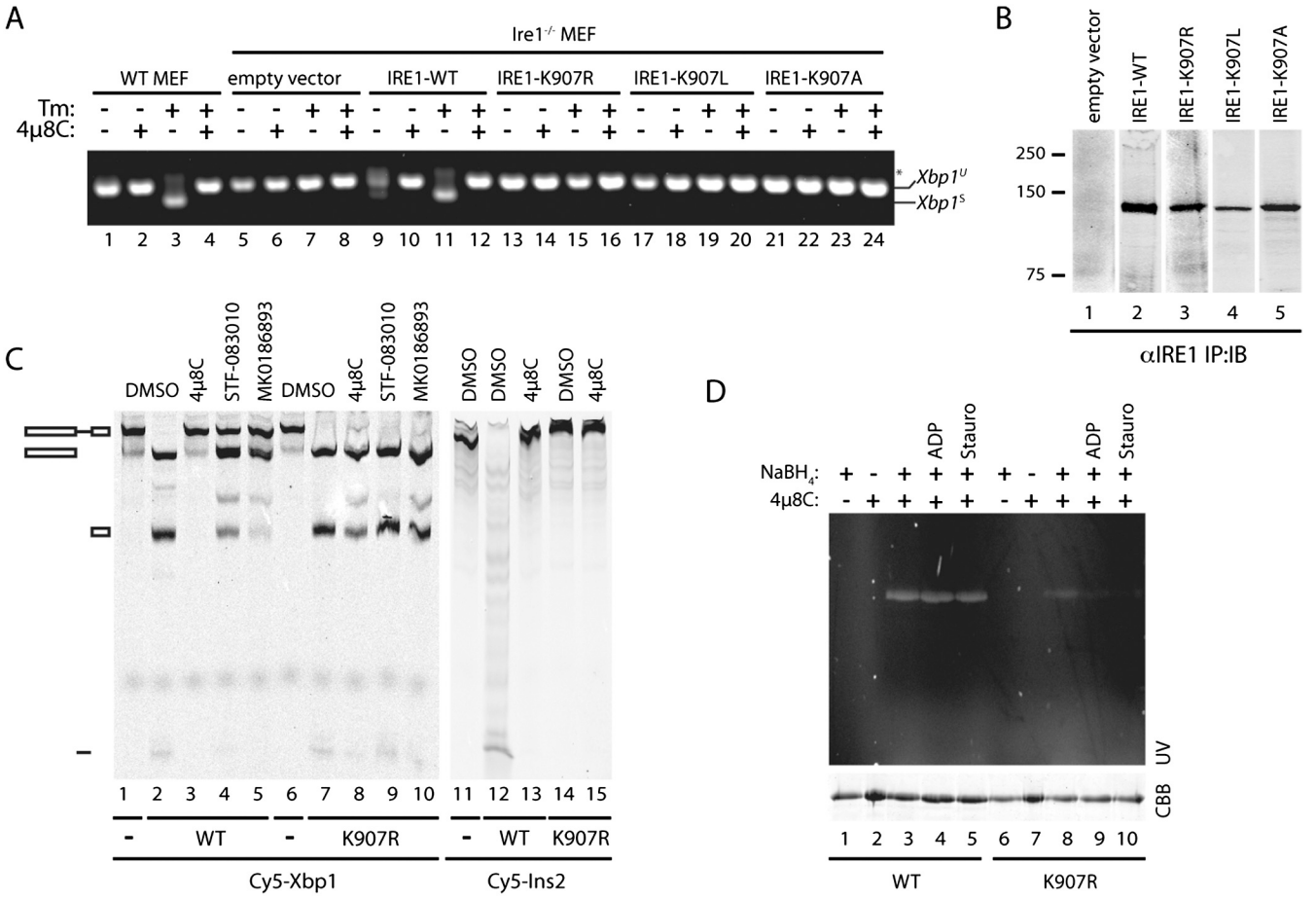

Fig. S9. The RNase activity of IRE1-K907R is refractory to 4μ8C. (*A*) RT-PCR of endogenous *Xbp1* from mouse Ire1$\alpha^{-/-}$ cells rescued by retroviral transduction with empty vector, wild-type, or the indicated mutant IRE1and cotreated with 2.5 μg/mL tunicamycin and 32 μM 4μ8C as indicated. Wild-type mouse embryonic fibroblasts serve as a reference cell line. Note the inability of these three mutants to rescue *Xbp1* splicing. (*B*) Immunoprecipitation followed by Western blotting of IRE1 protein from the cells shown in *A*. (*C*) Fluorogram of a denaturing (8M urea PAGE) RNA gel of fluorescent full-length *Xbp1* (*Left*) mRNA

derived from in vitro transcription subjected to cleavage over 30 min by either WT or IRE1^{K907R}, equalized for enzymatic activity and pretreated (20 min) with 20 μM of the indicated compounds. Note that while wild-type IRE1 is inhibited (albeit variably) by each of the inhibitors, the IRE1^{K907R} mutant is refractory to inhibition. (*Right*) The same assay with fluorescent full-length *Ins2* mRNA. Note that IRE1^{K907R} is unable to cleave this RNA species. (*D*) Fluorescent micrograph (excitation 340 nm, emission 450 nm) of an SDS-PAGE loaded with 2 μg of wild type or IRE1^{K907R}, preincubated with 2 mM ADP, 320 μM staurosporine or DMSO before exposure to 32 μM 4μ8C for 30 min with or without subsequent reduction by borohydride ($NaBH_4$), as indicated. Note lower level of binding of 4μ8C to IRE1^{K907R} (as compared to the wild type) and the ability of both ADP and staurosporine to block binding, indicating that it most likely results solely from binding at K^{599} in the kinase pocket.

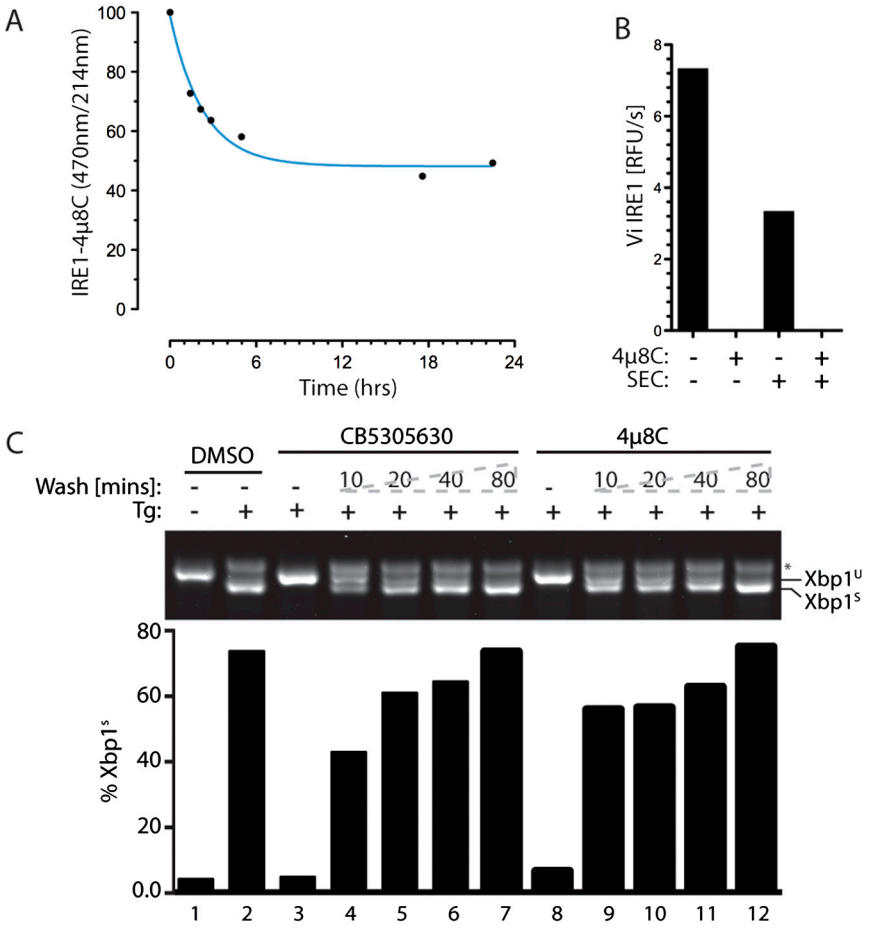

Fig. S10. Off-rate measurements for 4μ8C–IRE1. (*A*) The intensity of the IRE1-associated 4μ8C fluorescent peak of IRE1-4μ8C complex, resolved by size exclusion chromatography on a SEC3 column (normalized to protein content). Reactions (20 μL) containing 15 μM IRE1 and 100 μM 4μ8C were preincubated for 1 h in the absence of nucleotide prior to separation of IRE1 from free 4μ8C by size exclusion chromatography. The rate of dissociation was monitored by reapplication of aliquots from the purification to gel filtration at the indicated time points and the ratio of coeluting fluorescence (excitation 350 nm, emission 470 nm) to protein (absorbance 214 nm) plotted for each time point. The data were fitted to mono exponential decay with a half-life of 1.6 h. Modified protein retains approximately 50% fluorescence even after 24 h of incubation. The nature of this signal is not yet clear but may result from differing off-rates between the two modified sites in vitro. (*B*) RNase activity of 4μ8C or vehicle treated IRE1 measured using the FRET-derepression assay. Activity was assayed both before injection and after collection from the size exclusion column (SEC) (corresponding to the time zero point in *A*, above). Note that vehicle treated IRE1 recovered from the SEC column retains activity, whereas 4μ8C treated IRE1 is inactive even after separation from free 4μ8C, This indicates that the subsequently derived off-rates describe dissociation of a relevant complex. (*C*) Fluorescent stained agarose gel of an RT-PCR assay of the *Xbp1* mRNA from MEF cells. Where indicated, the cells were exposed to the ER stress-inducing agent thapsigargin in the absence or presence of the inhibitors CB5305630 or 4μ8C. In lanes 4–5 and 9–12, the inhibitor was washed away and replaced by fresh media (containing thapsigargin) and *Xbp1* splicing analyzed after the indicated period after the wash. Note the rapid reversal of the inhibitor's affect in vivo compared with stability of the complex in vitro.

Movie S1. Molecular dynamics simulation of the unmodified IRE1 (PDB ID code 3P23) conducted over 25 ns. Residues 870 to 939 shown highlighting Y^{882}, F^{889}, N^{906}, K^{907}, H^{910}.

Movie S1 (TIF)

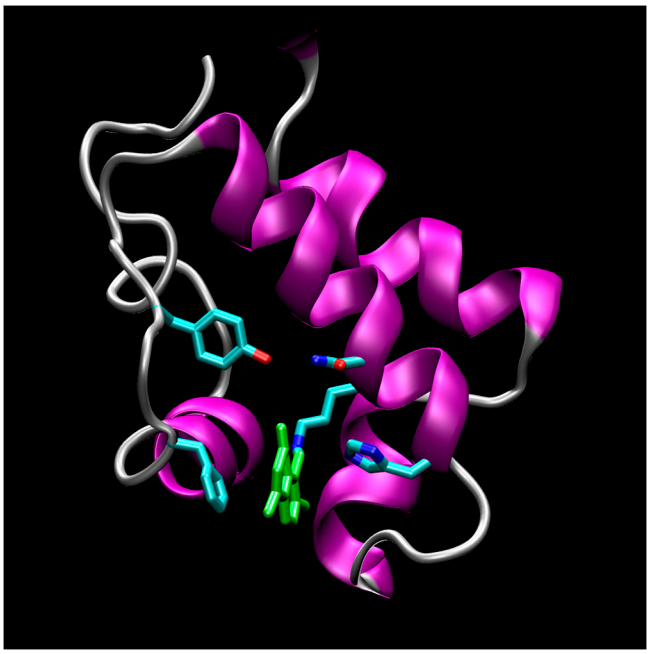

Movie S2. Twnety-five nanosecond MD simulation of IRE1 modified by 4μ8C at K^{907}. Residues 870 to 939 shown highlighting Y^{882}, F^{889}, N^{906}, K^{907}, H^{910}.

Movie S2 (TIF)

Table S1. Primers used in this study

Primer	Gene	Sequence (5′–3′)	Application
MmXBP1.14AS	Xbp1	GAATGCCCAAAAGGATATCAGACTC	XBP1 splicing
MmXBP1.19S	Xbp1	GGCCTTGTGGTTGAGAACCAGGAG	XBP1 splicing
MmHsp5a_1S	BiP	CCGAGGAGGAGGACAAGAAG	qPCR
MmHsp5a_2AS	BiP	CACATACGACGGCGTGATGC	qPCR
MmDdit3_1S	CHOP	GGAGCTGGAAGCCTGGTATGAG	qPCR
MmDdit3_2AS	CHOP	GCAGGGTCAAGAGTAGTGAAGG	qPCR
MmDerl1_1S	Derlin1	CCGGCCTACTTCTTCCTCTG	qPCR
MmDerl1_2AS	Derlin1	CGATGCAGATCCAGTTAAAGAG	qPCR
MmEdem1_1S	Edem1	TCTTCGGCTATGACAACTACATGG	qPCR
MmEdem1_2AS	Edem1	CTAACTTGACTGCCTTCTGGAAC	qPCR
MmERdj4_1S	ERdj4	CCATGAAGTACCACCCTGAC	qPCR
MmERdj4_2AS	ERdj4	CCTCTTTGTCCTTTGCCATTG	qPCR
MmP58_1S	ERdj6	CGCCTTATCACAGTTTCACG	qPCR
MmP58_2AS	ERdj6	CTAAGAAGACGGTAGCTCTCC	qPCR
MmHgsnat.1S	Hgsnat	TCTCCGCTTTCTCCATTTTG	qPCR
MmHgsnat.2AS	Hgsnat	CGCATACACGTGGAAAGTCA	qPCR
MmBlos1.1S	Blos1	CAAGGAGCTGCAGGAGAAGA	qPCR
MmBlos1.2AS	Blos1	GCCTGGTTGAAGTTCTCCAC	qPCR
MmScara3.1S	Scara3	TGCATGGATACTGACCCTGA	qPCR
MmScara3.2AS	Scara3	GCCGTGTTACCAGCTTCTTC	qPCR
MmPdgfrb.1S	Pdgfrb	AACCCCCTTACAGCTGTCCT	qPCR
MmPdgfrb.2AS	Pdgfrb	TAATCCCGTCAGCATCTTCC	qPCR
MmPmp22.1S	Pmp22	TGCGATACAGCAGAATGGAG	qPCR
MmPmp22.2AS	Pmp22	TTGGTGGCCAATACAAGTCA	qPCR
MmCol6.1S	Col6	TGCTCAACATGAAGCAGACC	qPCR
MmCol6.2AS	Col6	TTGAGGGAGAAAGCTCTGGA	qPCR
MmCyclophilinA_1S	Ppia	TTCCTCCTTTCACAGAATTATTCCA	qPCR
MmCyclophilinA_2AS	Ppia	CCGCCAGTGCCATTATGG	qPCR
T7-mIns2.1S	Ins2	TAATACGACTCACTATAGGGAGAAGCCCTAAGTGATCCGCTAC	in vitro RNase
mIns2.2AS	Ins2	GTGCTCATTCAAAGGTTTTATTCATTGC	in vitro RNase
T7.mXBP1.1S	Xbp1	TAATACGACTCACTATAGGGAGATCGAGATAGAAAGAAAGCCCG	in vitro RNase
mXBP1.14AS	Xbp1	GAATGCCCAAAAGGATATCAGACTC	in vitro RNase